

Porous plates at incidence

Chandan Bose, Callum Bruce and Ignazio Maria Viola*

School of Engineering, Institute for Energy Systems

University of Edinburgh, Edinburgh, EH9 3FB, UK

* i.m.viola@ed.ac.uk

March 23, 2023

Abstract

This paper investigates the effect of permeability on two-dimensional plates at incidences. The flow topology is investigated for Reynolds number (Re) values between 30 and 90, and the forces on the plate are discussed for $Re = 30$, where the wake is found to be steady for any value of the Darcy number (Da) and flow incidence (α). At $Re = 30$, for a plate normal to the stream and vanishing Da , the wake shows a vortex dipole with a stagnation point on the plate surface. With increasing Da , the separation between the vortex dipole and the plate increases; the vortex dipole shortens and is eventually annihilated at a critical Da . For any value of Da below the critical one, the vortex dipole disappears with decreasing α . However, at low Da , the two saddle-node pairs merge at the same α , annihilating the dipole; while at high Da , they merge at different α , resulting in a single recirculating region for intermediate incidences. The magnitude of lift, drag, and torque decrease with Da . Nevertheless, there exists a range of Da and α , where the magnitude of the plate-wise force component increases with Da , driven by the shear on the plate's pressure side. Finally, the analysis of the fluid impulse suggests that the lift and drag reduction with Da are associated with the weakening of the leading and trailing edge shear layer, respectively. The present findings will be directly beneficial in understanding the role of permeability on small porous wings.

1 Introduction

The flow past two-dimensional solid plates at different incidences with the free-stream velocity has been extensively studied experimentally (Fage & Johansen, 1927; Ingham *et al.*, 1990; Dennis *et al.*, 1993; Lam & Leung, 2005; Wu *et al.*, 2005; Taneda, 1968), numerically (Hudson & Dennis, 1985; Ingham *et al.*, 1990; Dennis *et al.*, 1993; In *et al.*, 1995; Saha, 2007; Zhang *et al.*, 2009; Saha, 2013; Hemmati *et al.*, 2018), as well as theoretically (Miyagi, 1978). Miyagi (1978) was one of the first to theoretically predict the minimum Re value to be zero for the flow separation around a plate normal to the stream to occur, giving rise to a standing vortex dipole. The thickness of the vortex dipole gradually becomes smaller with reducing Re , and the flow separates from the edge of the plate at any small Re value. At a critical Re value between 30 and 35 (whose exact value has not been reported), a Hopf bifurcation occurs, resulting in vortex shedding (Saha, 2007). The wake remains two-dimensional up to $Re \approx 200$.

In *et al.* (1995) numerically investigated the flow around a plate with zero thickness at an incidence α with the free stream and provided a map for flow patterns as a function of both α and Re . For a given Re and increasing α , the flow topology changes from attached flow at $\alpha \approx 0^\circ$ to a vortex dipole at $\alpha \approx 90^\circ$, and a single vortex at some intermediate values of α . Zhang *et al.* (2009) systematically studied the flow dynamics of a plate at incidences from 0° to 45° and $Re \leq 800$. The authors reported a route to transition from steady to chaotic flow through a sequential occurrence of period-doubling and quasi-periodic bifurcations.

The effect of permeability on the flow past porous plates has been investigated only at relatively high Re , i.e. in turbulent flow conditions, where a vortex dipole exists only in the time average sense (Castro, 1971; Graham, 1976). Recent numerical studies have focused on porous square cylinders (Dhinakaran & Ponmozhi, 2011; Anirudh & Dhinakaran, 2018; Ledda *et al.*, 2018; Tang *et al.*, 2020), porous circular cylinders (Yu *et al.*, 2011), porous spheres (Yu *et al.*, 2012; Ciuti *et al.*, 2021), and axisymmetric porous disks (Cummins *et al.*, 2017). Steiros & Hultmark (2018) developed an analytical model for predicting the drag on porous plates normal to the stream. Baddoo *et al.* (2021) extended unsteady thin aerofoil theory to aerofoils with generalised plate-wise porosity distributions.

The flow past these porous bodies is governed by Re , Da and the porosity (ϵ) (Darcy, 1856; Brinkman, 1949). A steady recirculation region exists for Re higher than the minimum value for flow separation to occur and an upper limit that depends on the body shape. This Re range is $O(1) < Re < O(10)$ (Ledda *et al.*, 2018). As Da increases, the recirculation region, which is attached to the body for vanishing Da , first detaches and then decreases in size until a certain critical value of Da . At higher Da values, there is no recirculation in the wake (Ledda *et al.*, 2018). In fact, there exists an upper limiting Da value, above which the flow is steady for any Re value, passing through the body without forming regions of recirculation in the wake (Ledda *et al.*, 2019).

Neither the effect of permeability nor the effect of flow incidences different from plate-normal on the vortex dipole and the fluid loads of porous plates at low Re , i.e. where the vortex dipole is stable, has been investigated in the existing literature. The present study takes up this analysis, primarily focusing on revealing how the flow topology and loads vary with the variation in permeability and incidence. To that end, in this paper, we numerically study the flow past a two-dimensional porous plate, with a width-to-thickness ratio $\chi = 10$, for a range of Da , and α values. We first study the steady-to-unsteady wake transition for a range of Re values, and then carry out a detailed flow-field and force analysis at $Re = 30$, where the wake remains steady throughout the chosen parametric space. The remainder of the paper is structured as follows. The numerical method, including detailed domain size and grid resolution independent study and solver validation, is presented in §2. The results and discussions are presented in §3. These include, first, the identification of the transition from a steady to an unsteady wake in the $Re - Da$ parameter space (§3.1); then the analysis of the flow-field past a plate normal to the stream (§3.2) and at different incidences with the stream (§3.3); finally, the analysis of how the forces and torque change with α and Da (§3.4) and the identification, using impulse theory, of the associated changes in the vorticity field (§3.5). The salient outcomes of this study are summarised in §4.

2 Methodology

We model a two-dimensional porous plate with width \hat{d} and thickness \hat{t} in a uniform stream of fluid with density $\hat{\rho}$ and velocity $\hat{\mathbf{u}}_\infty$. The hat over the symbols is used to indicate dimensional quantities. In the following, all quantities are made nondimensional using $\hat{\rho}$, \hat{d} and $\hat{\mathbf{u}}_\infty$. We define two different frames of reference (fig. 1a): (1) a global frame of reference $O(X, Y)$, where X and Y are parallel and orthogonal to $\hat{\mathbf{u}}_\infty$, respectively; and (2) a body fixed frame of reference $O(x, y)$, where x and y are in the plate-normal and plate-wise direction, respectively. The angle of attack α is defined as the complementary angle to the angle between the two frames of references, and thus $O(X, Y) = O(x, y)$ when $\alpha = 90^\circ$.

2.1 Governing equations and numerical approach

We solve, in the $O(X, Y)$ frame, the continuity equation and the Darcy-Brinkman-Forchheimer equation (Darcy, 1856; Brinkman, 1949; Joseph *et al.*, 1982), which are, in nondimensional form,

$$\nabla \cdot \mathbf{u} = 0, \quad (1)$$

$$\frac{1}{\epsilon} \frac{\partial \mathbf{u}}{\partial t} + \frac{1}{\epsilon^2} (\mathbf{u} \cdot \nabla) \mathbf{u} = -\nabla p + \frac{1}{\epsilon Re} \nabla^2 \mathbf{u} - \frac{1}{Re Da} \mathbf{u} - \frac{c_F}{\sqrt{Da}} |\mathbf{u}| \mathbf{u}, \quad (2)$$

where $\mathbf{u} = (u, v)$ is the nondimensional velocity vector with components u and v ; t is the nondimensional time; p is the nondimensional pressure; and c_F is a form-drag coefficient.

In this study, we consider $\epsilon = 0.95$ and $c_F = 0$, but different values are adopted to validate our results with those of other authors (see Sec. 2.4). We have developed a customised porous incompressible Navier-Stokes solver, `porousIcoFoam`, by modifying the `icoFoam` solver, available within the finite volume method based open-source library `OpenFOAM`. The spatial and temporal discretisations are second-order accurate. The Pressure Implicit with Splitting of Operator algorithm with a predictor step and two pressure correction loops has been used to couple the pressure and velocity equations. A preconditioned conjugate gradient iterative solver is used to solve the pressure equation, whereas a diagonal incomplete-Cholesky method is used for preconditioning. A preconditioned smooth solver is used to solve the pressure-velocity coupling equation, and the symmetric Gauss-Seidel method is used for preconditioning. The absolute error tolerance criteria for pressure and velocity are set to 10^{-6} . The simulations are run for a duration of 240 convective periods, \hat{d}/\hat{u}_∞ . This ensures convergence of the steady-state loads with relative errors smaller than 10^{-8} .

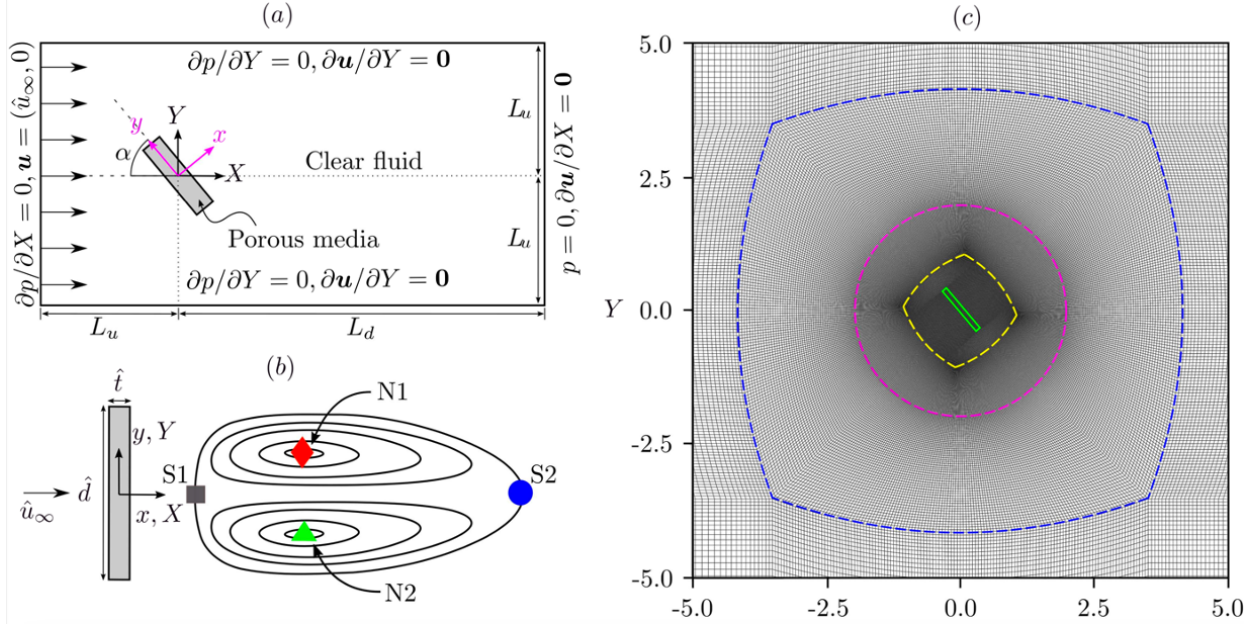


Figure 1: (a) Computational domain and boundary conditions (not to scale). (b) Schematic of the vortex dipole in the wake of a porous plate normal to the stream; saddle points S1, S2, and nodes N1, N2 are labelled. (c) Computational grid near the porous plate (green) at $\alpha = 50^\circ$. The external H-type grid transforms to O-type on the blue dashed line, and back to H-type on the yellow dashed line. The magenta dashed line is the interface about which the internal part of the grid is rotated for varying α .

2.2 Computational domain

The porous plate is placed within a rectangular computational domain with the edges parallel to the X and Y axis. The plate is placed at a distance $L_u = 20$ from the upstream and the lateral sides of the domain and $L_d = 80$ from the downstream edge (fig. 1a). At the upstream edge (inlet), we set $\mathbf{u} = (u_\infty, 0)$ and $\partial p / \partial X = 0$, while at the downstream edge (outlet), $p = 0$ and $\partial \mathbf{u} / \partial X = \mathbf{0}$. On the side edges, we apply a slip condition with $\partial p / \partial Y = 0$ and $\partial \mathbf{u} / \partial Y = \mathbf{0}$.

Equation 2 is solved both inside and outside of the porous plate. In the clear fluid region, outside of the plate, $\epsilon = 1$ and $Da \rightarrow \infty$, and thus eq. 2 simplifies into the incompressible Navier-Stokes equation for Newtonian fluids. At the edges of the plate, which is the interface between the clean fluid and the porous media, velocity, pressure, and stresses are conserved.

The domain is made of an external region, which is fixed for all simulations, and an internal region, which is rotated by α . The grid topology is shown in fig. 1c. The initial condition is a uniform flow on the whole domain with $\mathbf{u} = (u_\infty, 0)$ and $p = 0$.

2.3 Forces calculations

The fluid forces generated by the plate are computed from the pressure and shear forces acting on the edges of the plate, i.e. at the interface between the clean fluid and the porous media. Once the steady state is reached, the force is

$$\mathbf{F} = \oint_l p \mathbf{n} dl + \oint_l \mathbf{S} \cdot \mathbf{n} dl, \quad (3)$$

where \mathbf{n} is the unit vector locally normal to the plate perimeter l and pointing outwards; \mathbf{S} is the viscous stress tensor. It is noted that using the base $(\hat{\rho}, \hat{d}, \hat{u}_\infty)$, the force and torque coefficients are twice the nondimensional forces and torque. The lift, drag, and torque coefficients are $C_L = 2L$, $C_D = 2D$, and $C_M = 2M$, respectively. The torque is computed with respect to the origin of the frames and is positive anticlockwise.

2.4 Verification and validation

To estimate the modelling error due to the finite dimension of the domain, and the numerical error due to the finite cell size, we consider three cases and we compare the results with those of other authors. Case 1 is a steady simulation of the flow past a rectangular cylinder (i.e. $\chi = 1$) with $Re = 30$, $Da = 10^{-3}$, $\epsilon = 0.977$, $c_F = 0.148$. This case was modelled by Dhinakaran & Ponmozhi (2011) and by Anirudh & Dhinakaran (2018). Case 2 is an unsteady simulation of the same geometry ($\chi = 1$) with $Re = 75$, $Da = 10^{-6}$, $\epsilon = 0.629$, $c_F = 0.286$. Finally, Case 3 is that modelled by Ledda *et al.* (2018): a slender plate normal to the flow with $\chi = 10$, where $Re = 30$, $Da = 1.1 \times 10^{-3}$, $\epsilon = 0.650$, $c_F = 0$. For these three cases, we consider the errors in the estimates of C_D , the X -coordinate of the downstream saddle point S2, denoted by X_{S2} , and the Strouhal number St . We follow the verification and validation procedure outlined in Viola *et al.* (2013). This method was originally developed for yacht sails and was successively adopted for a wide range of applications, including the flow past the pappus of the dandelion diaspore (Cummins *et al.*, 2018), permeable disks (Cummins *et al.*, 2017), oscillating flapping foils (Wang *et al.*, 2018), wind turbines (Dai *et al.*, 2022), tidal turbines (Chen *et al.*, 2018), arrays of energy harvesters (Viola *et al.*, 2022), and ship hulls (Speranza *et al.*, 2019).

We consider four domains and three grids. The domains are built by progressively extending L_u and L_d by steps of 5 and 20, respectively. Specifically, $L_u = 10, 15, 20, 25$ and $L_d = 40, 60, 80, 100$ for domain D1 to D4, respectively. The grid spacing is the same for all domains, while the total number of grid points increases from D1 to D4.

The G2 and G3 grids are achieved by scaling each cell size of G1 by $\sqrt{2}$ and 2, respectively. Hence, the number of grid points along the domain boundaries is $n_X = 350, 492, 700$; $n_Y = 210, 295, 420$; and along the width and thickness of the plate is $n_d = n_t = 60, 84, 120$ for G1 to G3, respectively. The base grid G2 is used for the domain size investigation, and the base domain D3 is used for the grid resolution investigation.

We consider the relative change (ϕ) of a generic scalar with respect to the value computed with the base setting, with the relative change (h) of a source of error. The latter is chosen such that $h \rightarrow 0$ when the source of error vanishes. For example, Figure 2a shows the relative change of the drag coefficient, $\phi_{C_D} = C_D/C_{D_{base}}$, with the inverse of the relative domain size, $h = h_d = (L_u/L_{u_{base}})^{-1} = 20/L_u$. Figure 2b shows the relative change of S2's X -coordinate, $\phi_{X_{S2}} = X_{S2}/X_{S2_{base}}$, with the inverse of the relative number of cells, $h = h_g = (n_X/n_{X_{base}})^{-1} = 492/n_X$.

We fit the data with $\phi = ch^p + \phi_0$, where the coefficients c , p and ϕ_0 are computed with least square optimisation, and the standard deviation of the residuals is σ . The advantage of presenting the data in this form is that the extrapolated value ϕ_0 for $h \rightarrow 0$ is the expected true value of ϕ . For example, in Figure 2a and 2b, the extrapolated values ϕ_0 are ca. 0.96 and 1.005, that is about 4% lower and 0.05% higher than those computed with the base domain and grid. Hence, these latter values computed as $\delta = 1 - \phi_0$, are the estimated errors. This procedure is used for both the modelling error due to the domain size, and the numerical error due to the grid size. Table 1 shows the modelling errors δ_{C_D} , $\delta_{X_{S2}}$, and δ_{St} in the computation of C_D , X_{S2} and St , respectively, for Case 1 and Case 2.

For the numerical error due to the grid resolution, we compute the 95% confidence interval $[-U_\phi, U_\phi]$ centred on the value computed with the base setting (G2). The uncertainty U_ϕ is computed differently depending on the order of convergence p of the least square fit. Specifically, for $p \geq 0.95$, $U_\phi = 1.25|\delta_\phi| + \sigma$. For $p < 0.95$, $U_\phi = 1.5\Delta_\phi + \sigma$, where $\Delta_\phi = [\max(\phi) - \min(\phi)]/[1 - \min(h)/\max(h)]$. This estimate is valid for any $p < 0.95$, but when $-0.05 \leq p \leq 0.05$, the confidence interval can alternatively be centred on the mean of all the computed values, and the uncertainty estimated as $U_{\phi_{mean}} = 2(\sigma_\phi/\sqrt{N})$, where N is the number of step sizes used and σ_ϕ is the standard deviation of the distribution of ϕ . Here we adopt this second approach for St . Table 2 shows the uncertainty in the computation of C_D , X_{S2} and St for Case 1 and Case 2. The values of the p coefficient for the cases shown in table 2 are as follows. Case 1: $p_{C_D} = 0.57$, $p_{X_{S2}} = 1.56$. Case 2: $p_{C_D} = 0.02$, $p_{St} = 0.05$.

The values of C_D , X_{S2} and St computed with the base setting (D3, G2) are compared with those of other authors in table 3. The differences are consistent with the modelling errors due to the finite domain size and the numerical uncertainty. Note that Dhinakaran & Ponmozhi (2011) and Anirudh & Dhinakaran (2018) have used domains that are about half of D3 in size, and this is consistent with their higher estimates of C_D , X_{S2} and St .

Overall, the numerical and modelling error analysis reveals that the estimate of the forces and of the coordinates of topological points in the wake are predicted within a numerical uncertainty at 95% confidence level of 4.65% and 0.71%, respectively. The error due to the finite size of the domain is estimated at 5.07% and 0.89%, respectively.

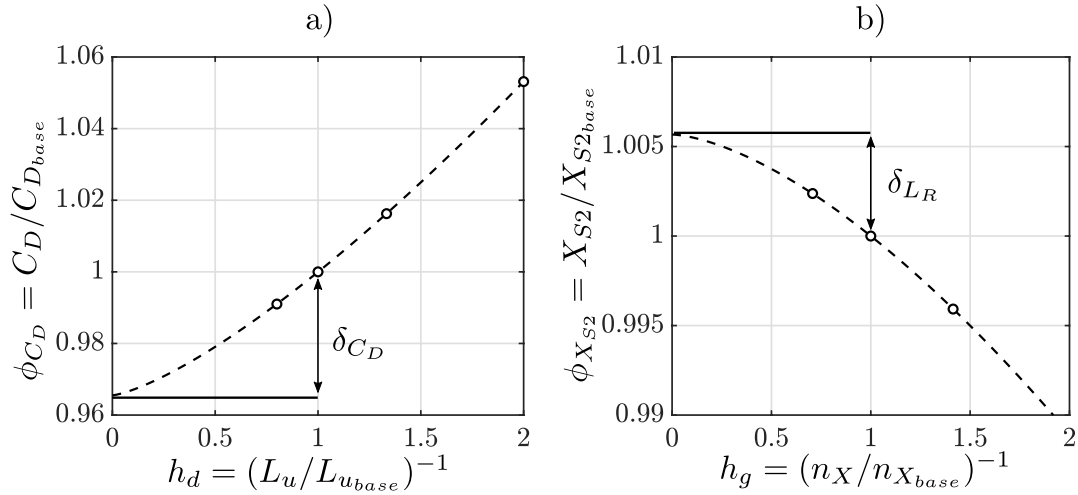


Figure 2: Case 1 convergence for a) C_D as a function of h_d and b) X_{S2} as a function of h_g .

Domain	h_d	Case 1				Case 2			
		C_D	$\delta_{C_D}(\%)$	X_{S2}	$\delta_{X_{S2}}(\%)$	C_D	$\delta_{C_D}(\%)$	St	$\delta_{St}(\%)$
D1	0.50	1.9444	8.76	1.9455	1.01	1.5244	6.14	0.1366	4.92
D2	0.75	1.8763	5.07	1.9431	0.89	1.4834	3.34	0.1337	2.73
D3	1.00	1.8463	3.45	1.9371	0.58	1.4664	2.18	0.1324	1.75
D4	1.25	1.8297	2.55	1.9321	0.32	1.4572	1.55	0.1318	1.30

Table 1: Modelling error due to the finite domain size for C_D , X_{S2} and St for a porous square cylinder. Case 1: $\chi = 1, Re = 30, Da = 10^{-3}, \epsilon = 0.977, c_F = 0.148$ (steady); Case 2: $\chi = 1, Re = 75, Da = 10^{-6}, \epsilon = 0.629, c_F = 0.286$ (unsteady).

Grid	h_g	Case 1		Case 2	
		$C_D, U_{C_D}(\%)$	$X_{S2}, U_{X_{S2}}(\%)$	$C_D, U_{C_D}(\%)$	$St, U_{St}(\%)$
G1	$\sqrt{2}$	1.8306, 4.65	1.9292, 1.22	1.4637, 0.21	0.1331, 1.27
G2	1	1.8463, 4.65	1.9371, 0.71	1.4664, 0.21	0.1324, 1.27
G3	$1/\sqrt{2}$	1.8592, 4.65	1.9417, 0.41	1.4609, 0.21	0.1303, 1.27

Table 2: Uncertainty due to finite grid resolution for C_D , X_{S2} and St for a porous square cylinder. Case 1: $\chi = 1, Re = 30, Da = 10^{-3}, \epsilon = 0.977, c_F = 0.148$ (steady); Case 2: $\chi = 1, Re = 75, Da = 10^{-6}, \epsilon = 0.629, c_F = 0.286$ (unsteady).

	Case 1		Case 2		Case 3	
	C_D	X_{S2}	C_D	St	C_D	X_{S2}
Anirudh and Dhinakaran (2018)	2.0021	1.9820	1.5639	0.1374	-	-
Dhinakaran and Ponmozhi (2011)	2.0255	1.9415	-	-	-	-
Sharma and Eswaran (2004)	-	-	1.5490	0.1370	-	-
Ledda et al. (2018)	-	-	-	-	1.86	2.15
Present study	1.8463	1.9371	1.4664	0.1324	1.77	2.07

Table 3: Present study results compared with three cases from the literature.

Case 1: $\chi = 1, Re = 30, Da = 10^{-3}, \epsilon = 0.977, c_F = 0.148$ (steady);
Case 2: $\chi = 1, Re = 75, Da = 10^{-6}, \epsilon = 0.629, c_F = 0.286$ (unsteady);
Case 3: $\chi = 4, Re = 30, Da = 1.1 \times 10^{-3}, \epsilon = 0.650, c_F = 0.0$.

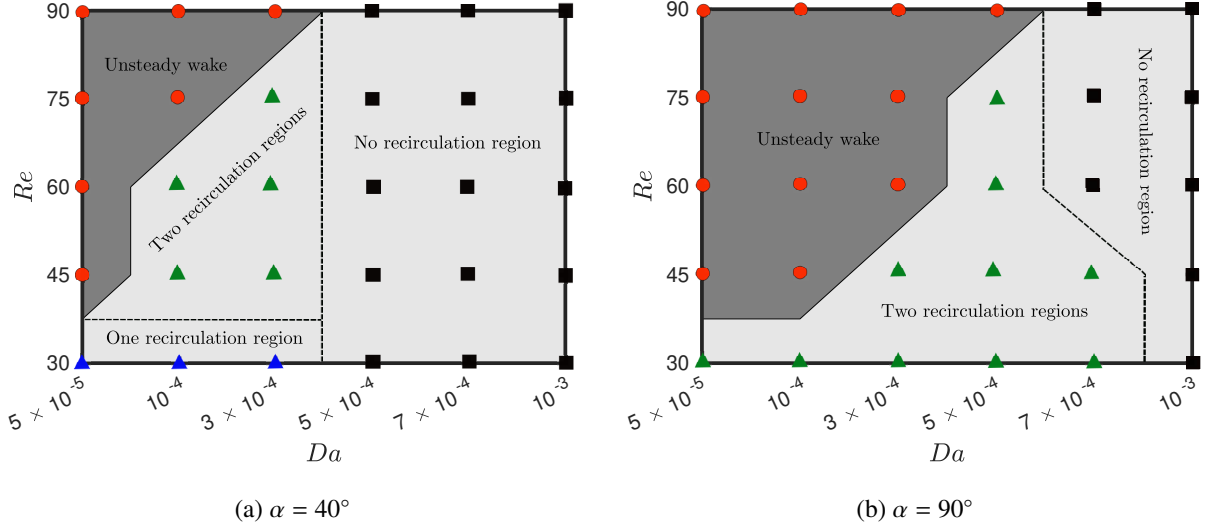


Figure 3: Map of the wake topology for a two-dimensional porous plate for a range of Reynolds and Darcy numbers. The light grey region and the deep grey region represent the steady and unsteady wake regions, respectively. The red circles, blue and green triangles, and black squares are indicative of unsteady vortex shedding, one and two recirculation regions, and no recirculation, respectively.

3 Results and Discussions

3.1 Steady-unsteady transition boundary

First, we investigate the Re and Da values for which the wake is steady and unsteady for flow incidences $\alpha = 40^\circ$ and 90° (figs. 3a and 3b, respectively). At both incidences, the critical Re value at which steady-unsteady transition occurs increases with Da , and decreases with α (solid line in figs. 3a and 3b). We also identify the transition between a steady wake with and without a recirculation region (dashed line in figs. 3a and 3b). At $\alpha = 90^\circ$, this transition occurs at $3 \times 10^{-4} < Da < 5 \times 10^{-4}$, and it seems independent of Re . Instead, at $\alpha = 40^\circ$, the critical Da at which this transition occurs decreases with Re . Finally, we observe that at $\alpha = 40^\circ$, wakes exists with either one and two recirculation regions, where the single recirculation region exists only at low Re and Da values. At $Re = 30$, the wake is always steady for any value of Da and α , and might present two, one, or no recirculation regions depending on Da and α . In the rest of the paper we investigate how the permeability allows switching between these three different flow typologies, and we focus on $Re = 30$ to ensure that the wake remains steady.

3.2 Porous plate normal to the stream

We first consider a plate at $Re = 30$ and $\alpha = 90^\circ$, where two recirculation regions occurs as showed in fig. 1b, and we investigate the effect of permeability. Figure 4a shows the X coordinate of the upstream (S1) and downstream (S2) saddle points versus Da , while fig. 4b shows C_D versus Da . For vanishing permeability ($Da \rightarrow 0$), the flow topology and the force tend asymptotically towards those of an impervious plate. The small differences between the results for an impervious plate and the asymptotic values for vanishing Da are attributed to the different numerical algorithms for porous and impervious bodies. As Da increases, S1 moves downstream and S2 moves upstream, shrinking the vortex dipole up to its annihilation at a critical Da , between 8×10^{-4} and 9×10^{-4} . This is also shown in figs. 4c-4e by means of the streamlines superimposed to the vorticity contour. The reduction in size and eventual annihilation of the vortex dipole coincides with a reduction in C_D . The C_D values obtained for an axisymmetric porous disc by Cummins *et al.* (2017) at $Re = 30$ are relatively higher than those obtained for a two-dimensional flat plate in this study. However, the trend of C_D variation with respect to Da is qualitatively similar in these two cases.

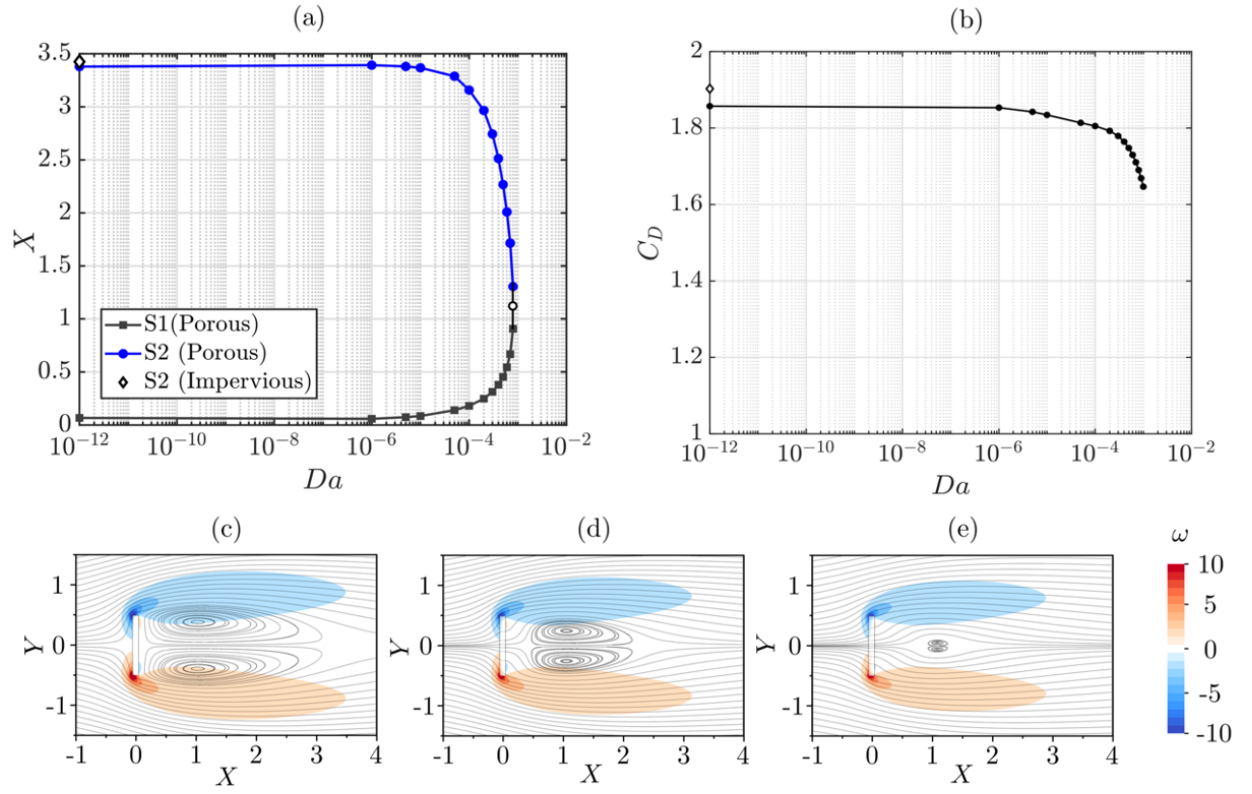


Figure 4: (a) Stream-wise coordinate of saddle points S1 and S2, and (b) drag coefficient versus the Darcy number for a two-dimensional porous plate with $\alpha = 90^\circ$ and $Re = 30$, where diamonds indicate the values for a solid plate at the same α and Re . Streamlines and vorticity field, ω , for (c) $Da = 5 \times 10^{-5}$, (d) $Da = 5 \times 10^{-4}$, and (e) $Da = 8 \times 10^{-4}$.

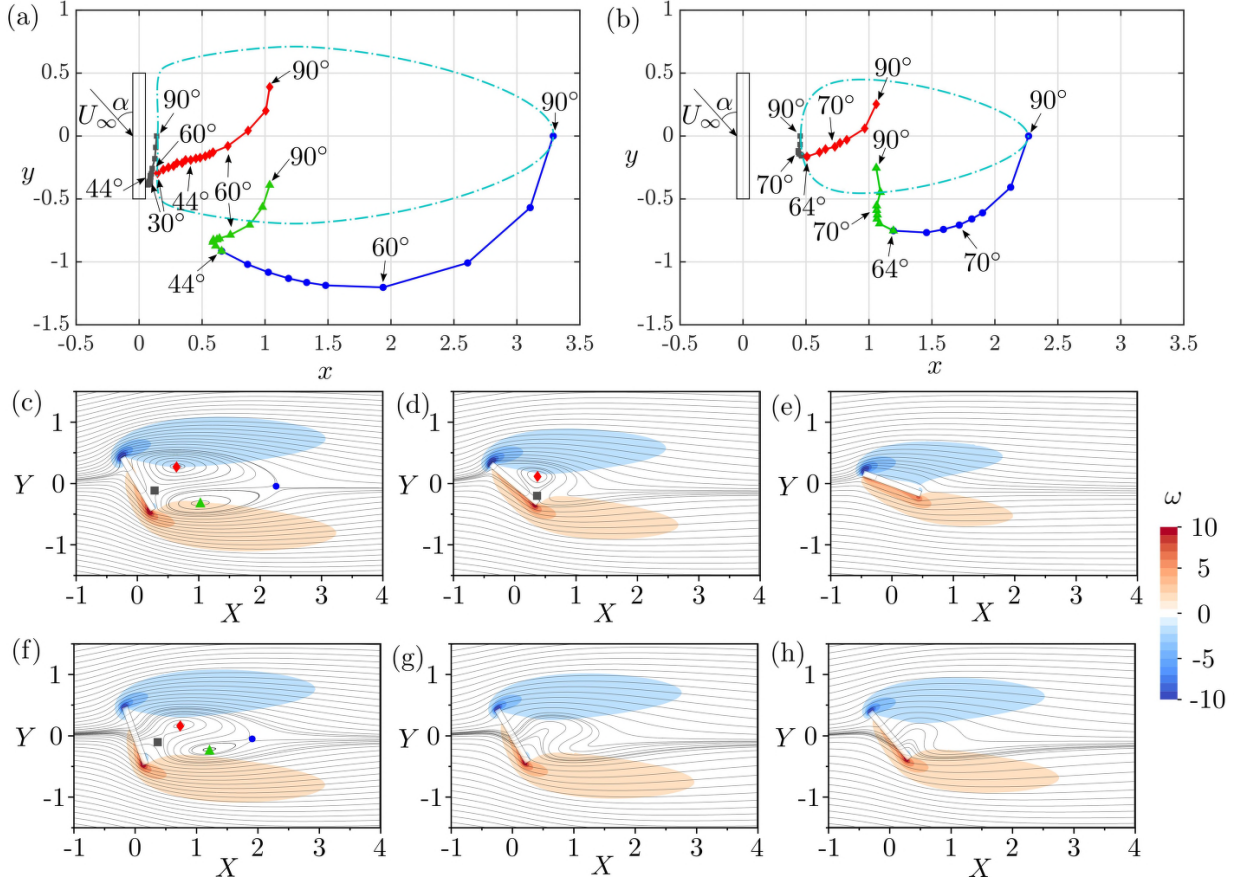


Figure 5: Position of nodes N1 (red diamond), N2 (green triangle), and saddle points S1 (grey square), S2 (blue circle) of a two-dimensional porous plate at $Re = 30$ for (a) $Da = 5 \times 10^{-5}$ and (b) $Da = 5 \times 10^{-4}$, where $\alpha = [90^\circ, 80^\circ, 70^\circ, 60^\circ, 54^\circ, 52^\circ, 50^\circ, 48^\circ, 46^\circ, 44^\circ, 42^\circ, 40^\circ, 38^\circ, 36^\circ, 34^\circ, 32^\circ, 30^\circ]$ in (a), $\alpha = [90^\circ, 80^\circ, 74^\circ, 72^\circ, 70^\circ, 68^\circ, 66^\circ, 64^\circ]$ in (b), and light blue dotted lines denote the closed streamline of the vortex dipole at $\alpha = 90^\circ$. Streamlines and vorticity field for $Da = 5 \times 10^{-5}$ and (c) $\alpha = 60^\circ$, (d) $\alpha = 40^\circ$, and (e) $\alpha = 20^\circ$. Streamlines and vorticity field for $Da = 5 \times 10^{-4}$ and (f) $\alpha = 70^\circ$, (g) $\alpha = 60^\circ$, and (h) $\alpha = 50^\circ$. When present, the positions of N1, N2, S1, and S2 are indicated.

3.3 Flow around a porous plate at incidence

We now turn our study to the effect of the angle of incidence on permeable plates. With decreasing α from 90° to 0° , the vortex dipole first becomes asymmetric and eventually annihilates. This occurs through different topological steps for low and high permeability values. For plates with low permeability, as well as for the impervious plates, the recirculating wake annihilates in two steps as α is decreased. Conversely, beyond a critical Da value, between 5×10^{-5} and 5×10^{-4} , the vortex dipole annihilates in a single step. This is shown in figs. 5a and 5b for low and high permeability cases ($Da = 5 \times 10^{-5}$ and 5×10^{-4}), respectively, where the body-fixed coordinates of the topological points (N1, N2, S1, and S2) are tracked for various incidences.

For the low-permeability case, with decreasing α , all four topological points move first downstream parallel with y and then turn towards the plate (fig. 5c). At $\alpha = 44^\circ$, N2 merges with S2, forming a distinct topological field, comprising only one re-circulation region with closed streamlines and negative circulation (fig. 5d). This topology exists for α as low as 30° , when N1 merges with S1 annihilating the re-circulation region (fig. 5e). In contrast, for the high-permeability case, the intermediate topology with only one re-circulation region does not exist (fig. 5f). Instead, both node-saddle point pairs merge at $\alpha = 64^\circ$ (fig. 5g). For lower values of α , the wake is characterised by tortuous streamlines with no closed re-circulation regions (fig. 5h).

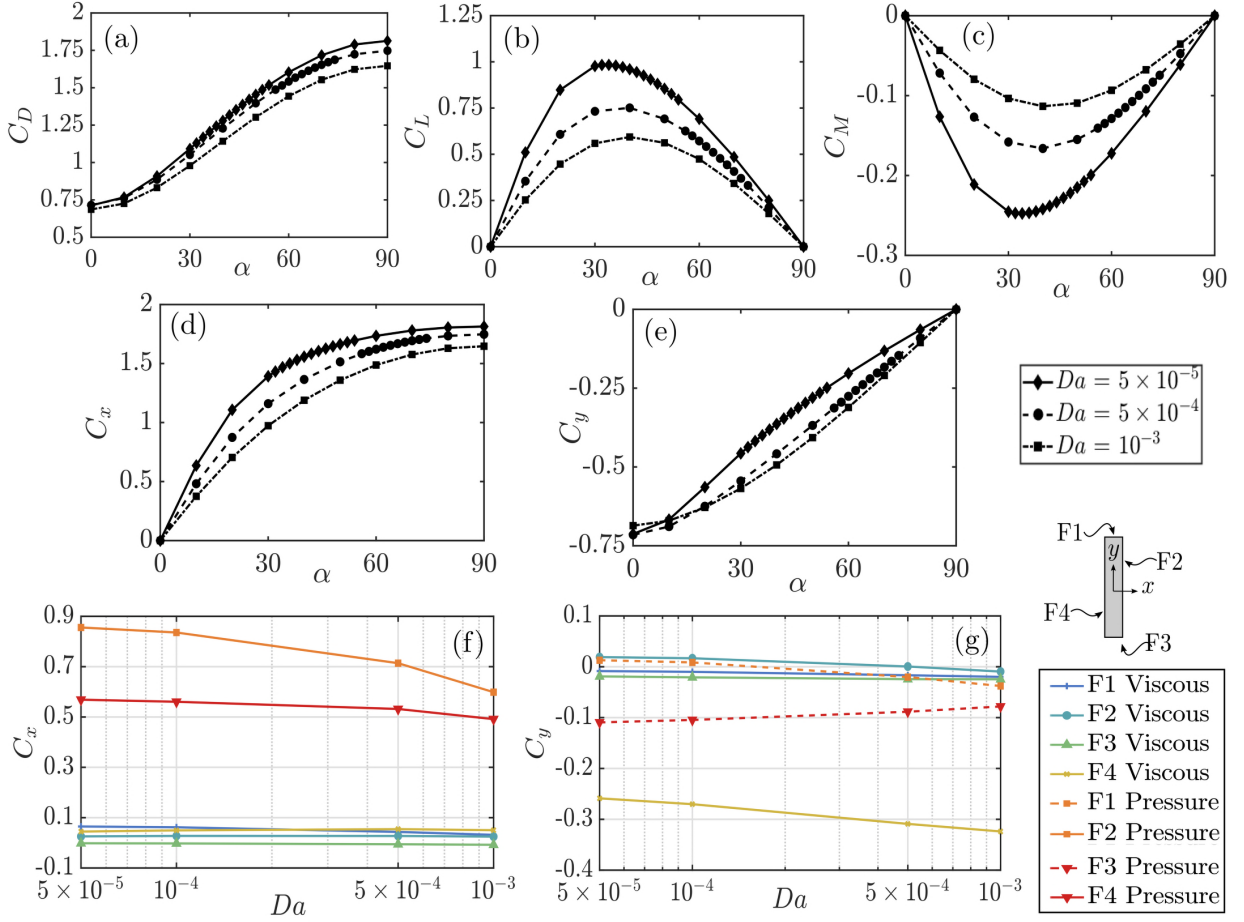


Figure 6: Coefficients of (a) drag, (b) lift (c) torque, (d) plate-normal force (e) plate-wise force for porous plates with three different permeability values versus the flow incidence. (f) Plate-normal and (g) plate-wise pressure and viscous force coefficients for each face (F1, F2, F3 and F4) of a porous plate at $\alpha = 40^\circ$ versus the Darcy number.

3.4 Forces and torque on a porous plate at incidence

Akin to the porous plate normal to the stream, both C_L and C_D decrease with increasing permeability at any α (fig. 6a and 6b). The lift and the torque vanish at $\alpha = 0^\circ$ and 90° , and their absolute value is maximum for the same critical incidence, α_{\max} , which increases with the permeability. Interestingly, at $Da = 5 \times 10^{-5}$, C_L and $|C_M|$ are maximum at $\alpha = 34^\circ$, where the wake is characterised by a single clockwise recirculation region; while at $Da = 10^{-3}$, C_L and $|C_M|$ are maximum near $\alpha = 40^\circ$, where there is no recirculation region. The C_D value, which increases monotonically from $\alpha = 0^\circ$ to 90° , shows a higher reduction with permeability at $\alpha = 90^\circ$ than 0° .

In the body-fixed frame of reference, while C_x decreases with Da (fig. 6c), $|C_y|$ increases with Da for any α between 20° and 90° ; see figs. 6d and 6e. To understand this result, we estimate the force components in the four faces of the porous plate, F1-F4, as defined in the inset of fig. 6. For each face, we consider the pressure and viscous components of C_x and C_y . The plate-normal force coefficient C_x is primarily driven by the suction on F2 and, to a lesser extent, by the pressure on F4 (fig. 6f). This is akin to a foil at incidence. Both the force contributions decrease with permeability, as expected. In contrast, C_y is primarily driven by the shear on F4 and to a lesser extent, by the suction on F3 (fig. 6g). The increase in shear on F4 with increasing Da is primarily responsible for the overall increase in C_y (fig. 6d).

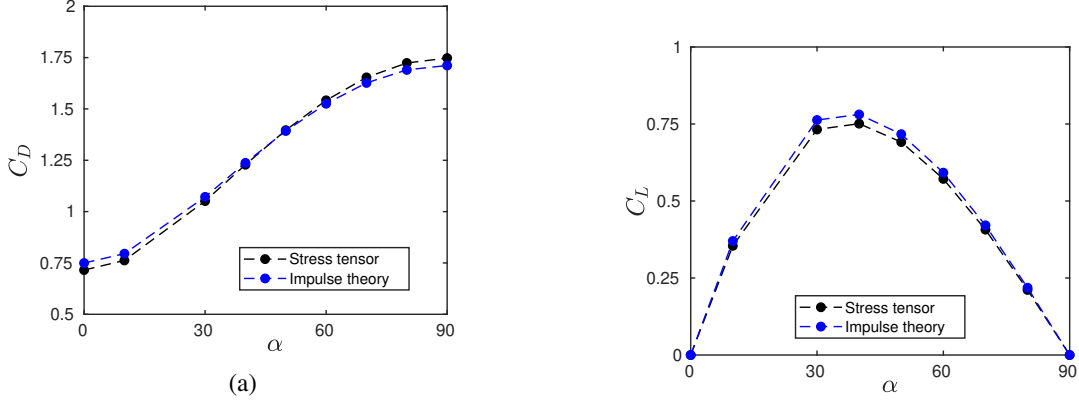


Figure 7: Lift and drag coefficients computed with the stress tensor and with impulse theory for different incidences at $Da = 5 \times 10^{-4}$.

	$Da = 5 \times 10^{-5}$		$Da = 5 \times 10^{-4}$		$Da = 10^{-3}$	
	C_L	C_D	C_L	C_D	C_L	C_D
Conventional	0.960	1.280	0.751	1.228	0.594	1.142
Impulse Theory	1.021	1.292	0.781	1.237	0.586	1.174

Table 4: Lift and drag coefficients computed with the stress tensor and with impulse theory for $\alpha = 40^\circ$ and three values of the Darcy number

3.5 Force calculation from the fluid impulse

We aim to investigate how the vorticity field around the plate varies with the permeability, and how these changes are correlated with the forces. For steady two-dimensional flows, the relationship between the vorticity field and the lift is given by the Kutta-Joukowski lift formula, which, in nondimensional form, is $L = -\Gamma$, where Γ is the nondimensional circulation, and $C_L = 2L$. For steady flow conditions, Γ should be computed as the integral of vorticity over a region enclosing the plate, such that the net flux of vorticity across the region boundary vanishes (Viola *et al.*, 2021). Here, we consider the integral of vorticity within the whole domain.

For steady two-dimensional flows, the nondimensional drag D is (Viola *et al.*, 2021)

$$D = - \int_W Y \omega \, dW, \quad (4)$$

where the line W orthogonally intersects the far wake, and $C_D = 2D$. Here we chose W as a stream-normal section of the domain at $X = 70$. The comparison between the force coefficients computed with the impulse theory and with the stress tensor (eq. 3) is shown in fig. 7.

From the Kutta-Joukowski lift formula ($L = -\Gamma$), we infer that the difference in the lift of two plates with different Da is proportional to the change in the integral of vorticity in the whole field. To gain insights on the underlying mechanism that leads to a lift change, we set to investigate which region experiences the greatest change in vorticity due to a change in permeability. We consider the plate at $\alpha = 40^\circ$ and three Da values: a low permeability case with $Da = 5 \times 10^{-5}$, where a single recirculation zone with negative circulation exists (fig. 5d); a high permeability case with $Da = 5 \times 10^{-4}$, where there are no close recirculation regions (fig. 5g); and the maximum permeability case, investigated in this study, with $Da = 10^{-3}$. Here, the terms ‘low-permeability’ and ‘high-permeability’ are used consistently with the the previous sections. The vorticity fields of the low, high, and max permeability cases are denoted as ω_L , ω_H , and ω_M , respectively. The lift and drag coefficients for these three cases are shown in table 4.

The spatial distributions of the differential vorticity fields $\omega_H - \omega_L$ and $\omega_M - \omega_H$ (figs. 8a and 8b, respectively) show how each fluid region contribute to the change in the lift. Four distinct regions are observed: two associated with the leading and trailing edge shear layers, and two associated with the suction and pressure side of the plate. For example, in fig. 8, the threshold value of $|\omega_t| = 0.48$ is used to clearly identify the four regions. The

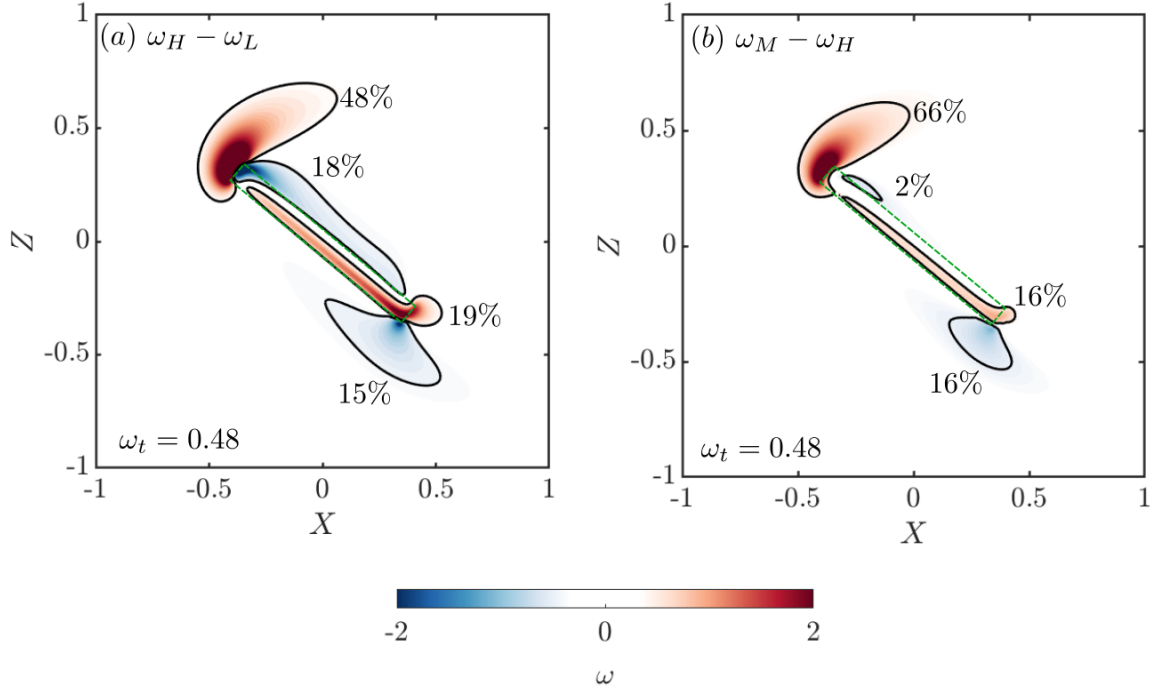


Figure 8: Differential vorticity fields for the porous plate at $\alpha = 40^\circ$: (a) $\omega_H - \omega_L$, and (b) $\omega_M - \omega_H$. The percentage values show the relative circulation of the four regions identified by the isolines of differential vorticity $|\omega| = 0.48$.

vorticity within each region is integrated to compute the contribution to the total change in circulation, and thus lift. The percentage values indicate the absolute circulation fraction of each region over the summation of the absolute circulation of all four regions. It is noted that these percentage values are about independent of the threshold value ω_t . For both $\omega_H - \omega_L$ and $\omega_M - \omega_H$, the integral of the change of vorticity near the leading-edge is substantially higher than the change of vorticity in the other three marked flow regions. Hence, we conclude that the change in the strength of the leading edge shear layer is the main driver for the lift change. Furthermore, its dominant role compared to that of the two shear layers along the chord, and that of the trailing edge shear layer, increases with Da (e.g. from 48% to 66% in fig. 8).

To investigate how changes in the vorticity field due to the increased permeability are correlated with the loss of drag, we consider the first moment of vorticity in the stream-wise direction, $Y\omega$, whose integral along the line W is the drag (eq. 4). The leading- and trailing-edge vortex sheet results in two peaks (fig. 9a), whose amplitude decreases with permeability, while their width is constant. This result suggests that the drop in drag with an increased permeability is primarily due to the weakening of the strength of the vortex sheet and not, for example, by the reduction of the width of the wake. To quantify the relative effect of the leading- and trailing-edge vortex sheet strength on the change of drag coefficient, we consider the difference of the first moment of vorticity in the stream-wise direction for the $\omega_L - \omega_H$ and $\omega_H - \omega_M$ cases; see fig. 9b. The figure also shows the zeros of the functions $Y|\Delta\omega| = 0$ for $\Delta\omega = \omega_L - \omega_H$ (A_1 - D_1), and for $\Delta\omega = \omega_H - \omega_M$ (A_2 - D_2). By computing the integral along Y between consecutive zeros, we find that, for the $\omega_L - \omega_H$ case, the changes in C_D due to the weakening of leading- and trailing-edge vortex sheet are 0.0251 and 0.0555, respectively; whereas, the corresponding changes in C_D for the $(\omega_H - \omega_M)$ case are 0.0192 and 0.0577, respectively. These results suggest that, with the increased permeability, the weakening of the trailing-edge vortex sheet is more significant than that of the leading-edge vortex sheet on the drag reduction.

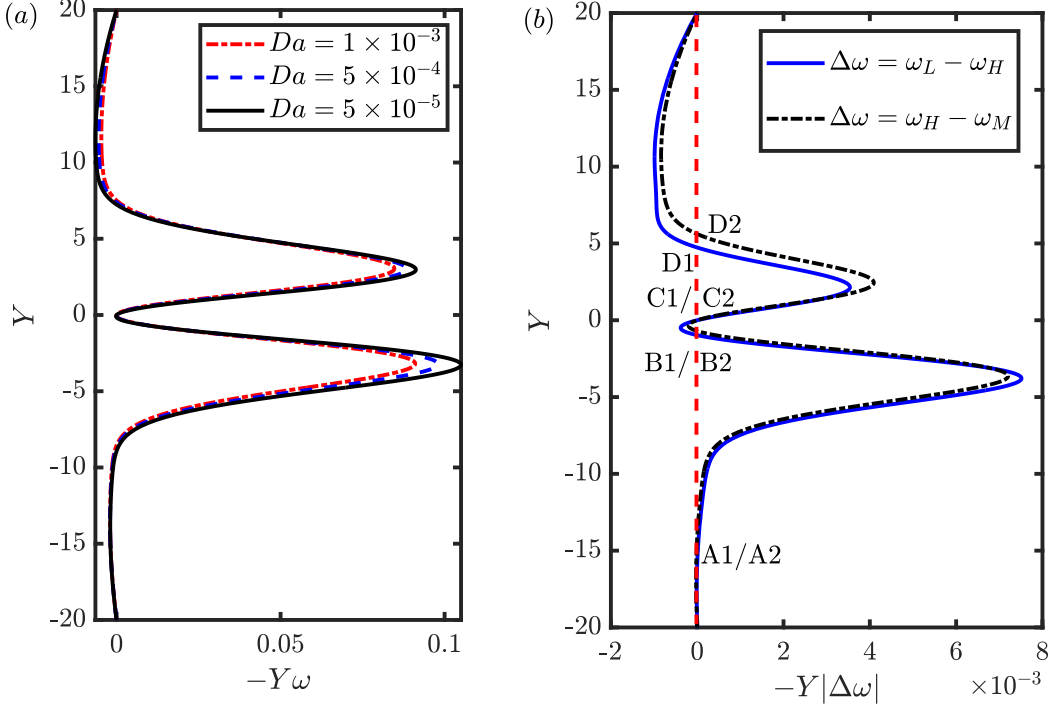


Figure 9: (a) Stream-wise component of the negative first moment of the vorticity field $-Y\omega$ and (b) the difference of the negative first moment of the vorticity field $-Y|\Delta\omega|$ for the $\omega_L - \omega_H$ and $\omega_H - \omega_M$ cases along the $X = 70$ line for $\alpha = 40^\circ$ and $Da = 5 \times 10^{-5}$, 5×10^{-4} and 10^{-3} .

4 Conclusions

The flow past a two-dimensional porous plate is investigated for different values of the permeability (Da) and flow incidence (α). The flow typology is investigated for Reynolds number (Re) values between 30 and 90, while a detailed analysis of the forces is undertaken at $Re = 30$, where the wake is found to be steady for any Da and α . An incompressible Navier-Stokes solver of the open-source library OpenFOAM has been modified to solve for the Darcy-Brinkman-Forchheimer equation in the porous region.

For a porous plate normal to the stream, below a critical Darcy number, between 8×10^{-4} and 9×10^{-4} , a vortex dipole with two saddles and two nodes is formed in the wake. With increasing Da , the separation of the dipole from the plate increases and both the pairs of topological points merge, eventually annihilating the dipole.

With decreasing α from 90° to 0° , the vortex dipole annihilation process is distinct for low and high permeability cases ($Da = 5 \times 10^{-5}$ and $Da = 5 \times 10^{-4}$). For the former, first, the downstream saddle and node merge, forming a single recirculating region with negative circulation. With decreasing α further, the upstream node and saddle merge, annihilating the recirculating region. Conversely, the four topological points for highly permeable plates merge at the same critical incidence. Lift, drag, and torque decrease in magnitude with Da , but there exists a range of α and Da where the plate-wise force component increases in magnitude because of the shear force on the pressure side of the plate.

The steady and unsteady transition boundaries are compared for a representative value of $\alpha = 40^\circ$ and the stream-normal condition. It is observed that the wake remains steady for higher Re and lower Da values when the porous plate is at an incidence as compared to the stream-normal condition.

The analysis of the rate of change of the flow impulse suggests that effect of an increased permeability is to decrease the lift by weakening the leading-edge shear layer, and to decrease the drag by weakening the trailing edge shear layer.

5 Acknowledgements

This work was funded by the ERC Consolidator Grant ‘Dandidrone’ (101001499), and Callum Bruce’s scholarship was funded by the EPSRC grant EP/S023801/1.

6 Declaration of interests

The authors report no conflict of interest.

References

- ANIRUDH, K & DHINAKARAN, S 2018 On the onset of vortex shedding past a two-dimensional porous square cylinder. *Journal of Wind Engineering and Industrial Aerodynamics* **179**, 200–214.
- BADDOO, PETER J, HAJIAN, ROZHIN & JAWORSKI, JUSTIN W 2021 Unsteady aerodynamics of porous aerofoils. *Journal of Fluid Mechanics* **913**.
- BRINKMAN, HENDRIK C 1949 A calculation of the viscous force exerted by a flowing fluid on a dense swarm of particles. *Flow, Turbulence and Combustion* **1** (1), 27–34.
- CASTRO, IP 1971 Wake characteristics of two-dimensional perforated plates normal to an air-stream. *Journal of Fluid Mechanics* **46** (3), 599–609.
- CHEN, BING, SU, SHAOSHUAI, VIOLA, IGNAZIO MARIA & GREATER, CLIVE A 2018 Numerical investigation of vertical-axis tidal turbines with sinusoidal pitching blades. *Ocean Engineering* **155**, 75–87.
- CIUTI, M, ZAMPOGNA, GA, GALLAIRE, F, CAMARRI, S & LEDDA, PG 2021 On the effect of a penetrating recirculation region on the bifurcations of the flow past a permeable sphere. *Physics of Fluids* **33** (12), 124103.
- CUMMINS, CATHAL, SEALE, MADELEINE, MACENTE, ALICE, CERTINI, DANIELE, MASTROPAOLO, ENRICO, VIOLA, IGNAZIO MARIA & NAKAYAMA, NAOMI 2018 A separated vortex ring underlies the flight of the dandelion. *Nature* **562** (7727), 414–418.
- CUMMINS, CATHAL, VIOLA, IGNAZIO MARIA, MASTROPAOLO, ENRICO & NAKAYAMA, NAOMI 2017 The effect of permeability on the flow past permeable disks at low reynolds numbers. *Physics of Fluids* **29** (9), 097103.
- DAI, WEIDONG, BROGLIA, RICCARDO & VIOLA, IGNAZIO MARIA 2022 Mitigation of rotor thrust fluctuations through passive pitch. *Journal of Fluids and Structures* **112**, 103599.
- DARCY, HENRY 1856 *Les fontaines publiques de la ville de Dijon: Exposition et application des principes à suivre et des formules à employer dans les questions de distribution d’eau: Ouvrage terminé par un appendice relatif aux fournitures d’eau de plusieurs villes, au filtrage des eaux et à la fabrication des tuyaux de fonte, de plomb, de tôle et de bitume*, vol. 2. V. Dalmont.
- DENNIS, SCR, QIANG, WANG, COUTANCEAU, M & LAUNAY, J-L 1993 Viscous flow normal to a flat plate at moderate reynolds numbers. *Journal of Fluid Mechanics* **248**, 605–635.
- DHINAKARAN, S & PONMOZHI, J 2011 Heat transfer from a permeable square cylinder to a flowing fluid. *Energy Conversion and Management* **52** (5), 2170–2182.
- FAGE, ARTHUR & JOHANSEN, FC 1927 On the flow of air behind an inclined flat plate of infinite span. *Proceedings of the Royal Society of London. Series A, Containing Papers of a Mathematical and Physical Character* **116** (773), 170–197.
- GRAHAM, JMR 1976 Turbulent flow past a porous plate. *Journal of Fluid Mechanics* **73** (3), 565–591.

- HEMMATI, ARMAN, WOOD, DAVID H & MARTINUZZI, ROBERT J 2018 On simulating the flow past a normal thin flat plate. *Journal of Wind Engineering and Industrial Aerodynamics* **174**, 170–187.
- HUDSON, JD & DENNIS, SCR 1985 The flow of a viscous incompressible fluid past a normal flat plate at low and intermediate reynolds numbers: the wake. *Journal of Fluid Mechanics* **160**, 369–383.
- IN, KM, CHOI, DO HYUNG & KIM, MU 1995 Two-dimensional viscous flow past a flat plate. *Fluid Dynamics Research* **15** (1), 13.
- INGHAM, DB, TANG, TAO & MORTON, BR 1990 Steady two-dimensional flow through a row of normal flat plates. *Journal of Fluid Mechanics* **210**, 281–302.
- JOSEPH, DANIEL D, NIELD, DONALD A & PAPANICOLAOU, GEORGE 1982 Nonlinear equation governing flow in a saturated porous medium. *Water Resources Research* **18** (4), 1049–1052.
- LAM, KM & LEUNG, MICHAEL YH 2005 Asymmetric vortex shedding flow past an inclined flat plate at high incidence. *European Journal of Mechanics-B/Fluids* **24** (1), 33–48.
- LEDDA, PIER GIUSEPPE, SICONOLFI, LORENZO, VIOLA, FRANCESCO, CAMARRI, SIMONE & GALLAIRE, FRANÇOIS 2019 Flow dynamics of a dandelion pappus: A linear stability approach. *Physical Review Fluids* **4** (7), 071901.
- LEDDA, PIER GIUSEPPE, SICONOLFI, LORENZO, VIOLA, FRANCESCO, GALLAIRE, FRANÇOIS & CAMARRI, SIMONE 2018 Suppression of von kármán vortex streets past porous rectangular cylinders. *Physical Review Fluids* **3** (10), 103901.
- MİYAGI, TOSHIO 1978 Standing vortex-pair behind a flat plate normal to uniform flow of viscous fluid. *Journal of the Physical Society of Japan* **45** (5), 1751–1755.
- SAHA, ARUN K 2007 Far-wake characteristics of two-dimensional flow past a normal flat plate. *Physics of Fluids* **19** (12), 128110.
- SAHA, ARUN K 2013 Direct numerical simulation of two-dimensional flow past a normal flat plate. *Journal of Engineering Mechanics* **139** (12), 1894–1901.
- SPERANZA, NICOLA, KIDD, BARRY, SCHULTZ, MICHAEL P & VIOLA, IGNAZIO MARIA 2019 Modelling of hull roughness. *Ocean Engineering* **174**, 31–42.
- STEIROS, KONSTANTINOS & HULTMARK, MARCUS 2018 Drag on flat plates of arbitrary porosity. *Journal of Fluid Mechanics* **853**.
- TANEDA, SADATOSHI 1968 Standing twin-vortices behind a thin flat plate normal to the flow(standing twin vortices in wake behind thin flat plate normal to flow visualized by al dust, noting karman vortex street). *Kyushu University, Research Institute for Applied Mechanics Reports* **16** (54), 155–163.
- TANG, TINGTING, YU, PENG, YU, SHIMIN, SHAN, XIAOWEN & CHEN, HUISU 2020 Connection between pore-scale and macroscopic flow characteristics of recirculating wake behind a porous cylinder. *Physics of Fluids* **32** (8), 083606.
- VIOLA, IGNAZIO MARIA, ARREDONDO-GALEANA, ABEL & PISETTA, GABRIELE 2021 The force generation mechanism of lifting surfaces with flow separation. *Ocean Engineering* **239**, 109749.
- VIOLA, IGNAZIO MARIA, BOT, PATRICK & RIOTTE, MATTHIEU 2013 On the uncertainty of cfd in sail aerodynamics. *International Journal for Numerical Methods in Fluids* **72** (11), 1146–1164.
- VIOLA, IGNAZIO MARIA, GAO, ZHI & SMITH, JAMES 2022 Use of streamnormal forces within an array of tidal power harvesters. *Plos One* **17** (7), e0270578.
- WANG, ENHAO, RAMESH, KIRAN, KILLEN, SHAUN & VIOLA, IGNAZIO MARIA 2018 On the nonlinear dynamics of self-sustained limit-cycle oscillations in a flapping-foil energy harvester. *Journal of Fluids and Structures* **83**, 339–357.

- WU, SJ, MIAU, JIUN-JIH, HU, CC & CHOU, JH 2005 On low-frequency modulations and three-dimensionality in vortex shedding behind a normal plate. *Journal of Fluid Mechanics* **526**, 117–146.
- YU, PENG, ZENG, YAN, LEE, THONG SEE, CHEN, XIAO BING & LOW, HONG TONG 2011 Steady flow around and through a permeable circular cylinder. *Computers & Fluids* **42** (1), 1–12.
- YU, PENG, ZENG, YAN, LEE, THONG SEE, CHEN, XIAO BING & LOW, HONG TONG 2012 Numerical simulation on steady flow around and through a porous sphere. *International Journal of Heat and Fluid Flow* **36**, 142–152.
- ZHANG, JIE, LIU, NAN-SHENG & LU, XI-YUN 2009 Route to a chaotic state in fluid flow past an inclined flat plate. *Physical Review E* **79** (4), 045306.